

Kinematics of Milky Way Satellites in a Lambda Cold Dark Matter Universe

Louis E. Strigari¹, Carlos S. Frenk² and Simon D. M. White³

¹*Kavli Institute for Particle Astrophysics and Cosmology, Stanford University, Stanford, CA 94305 USA*

²*Institute for Computational Cosmology, Dep. of Physics, Univ. of Durham, South Road, Durham DH1 3LE, UK*

³*Max-Planck-Institut für Astrophysik, Karl-Schwarzschild-Straße 1, 85740 Garching bei München, Germany*

6 November 2021

ABSTRACT

We investigate whether the subhalos of Λ CDM galaxy halos have potentials consistent with the observed properties of Milky Way satellites, particularly those with high-quality photometric and kinematic data: Fornax, Leo I, Sculptor, Sextans, and Carina. We compare spherical models with isotropic velocity dispersion tensors to the observed, circularly averaged star counts, line-of-sight velocity dispersion profiles and line-of-sight velocity distributions. We identify subhalos within the six high-resolution dark matter halos of the Aquarius Project for which the spherically averaged potentials result in excellent fits to each of the five galaxies. In particular, our simple one-integral models reproduce the observations in the inner regions, proving that these data are fully consistent with Λ CDM expectations and do not require cored dark matter distributions. For four of the five satellites the fits require moderately cusped *stellar* density profiles. The star count data for Leo I, however, do require a cored distribution of star counts. Current data suggest that these five satellites may be hosted by Λ CDM subhalos with maximum circular velocities in the range 10 to 30 km s⁻¹.

Key words: Dark Matter: Galaxies

1 INTRODUCTION

The internal dynamics of the dwarf spheroidal (dSph) satellite galaxies of the Milky Way (MW) offer perhaps the best prospects for investigating the properties of the dark matter in the nearby universe. These galaxies are dominated by dark matter and the brightest of them are sufficiently close that high-precision line-of-sight velocities for large samples of their stars can be measured using high-resolution, multi-object spectroscopy (Walker et al. 2009). The current datasets represent an improvement upon the earliest such observations (Aaronson 1983; Mateo et al. 1993) by factors of tens to thousands. Analysis of the kinematic data, in combination with improved photometric measurements, have not only confirmed earlier indications that the classical dSphs are dark matter dominated, but have also revealed the surprising property that their mean central densities are similar even though their luminosities span a very wide range of values (Mateo 1998; Walker et al. 2007; Gilmore et al. 2007; Strigari et al. 2008).

Current cosmogonic theory makes strong predictions for the internal structure of dark matter halos. N-body simulations of halo formation in hierarchical clustering cosmologies have shown that halos develop strongly cusped den-

sity profiles which are almost independent of halo mass and cosmological parameters (Navarro et al. 1996, 1997). Subsequent simulations have confirmed this result (e.g. Navarro et al. 2010; Stadel et al. 2009), showing, in addition, that cuspy profiles are retained even after halos fall into larger ones and suffer extensive tidal stripping (Kazantzidis et al. 2006; Springel et al. 2008). Thus, to the extent that the dark matter distributions in the inner parts of halos have not been significantly disturbed by the galaxies forming within them, halo profiles offer a strong and direct test of the Λ CDM cosmogony in a regime not probed by microwave background and large-scale structure data.

An in-depth analysis of the central regions of Milky Way satellites is particularly important given that a number of recent studies of the structure of these galaxies have claimed that shallow central density profiles provide a better description of their dark matter halos than the cuspy profiles characteristic of Λ CDM (Goerdts et al. 2006; Sánchez-Salcedo et al. 2006; Gilmore et al. 2007). Models with dark matter core radii of ~ 100 pc have been shown to provide good fits to the kinematic data sets of the classical dSphs (Angus & Diaferio 2009). If confirmed, the shallow cores suggested by these studies might indicate a lower

central phase-space density than expected if the dark matter is a cold collisionless particle (Tremaine & Gunn 1979; Hogan & Dalcanton 2000).

Kinematic studies typically treat dSph galaxies as spherical, dynamically equilibrated systems. With these simple assumptions there is a strong degeneracy between the statistics of stellar orbits (i.e. whether velocity dispersions are isotropic, or are radially or tangentially biased) and the shape of the stellar and dark matter density profiles (e.g. Evans et al. 2009). This ambiguity is reflected in the broad range of models used in recent attempts to constrain the dark matter density profiles of the dSphs (Strigari et al. 2008; Lokas 2009; Walker et al. 2009; Wolf et al. 2009). The intrinsic parameter degeneracies of the models cast doubt on the robustness of inferences favoring cored or cuspy central density profiles, even given the high-quality data that are now available (Strigari et al. 2006; Walker et al. 2009). Breaking these degeneracies may only be possible by exploiting additional observational constraints, for example, through measurement of internal stellar proper motions (Wilkinson et al. 2002; Strigari et al. 2007).

Motivated by the simple question of whether the observed dSphs are kinematically consistent with the Λ CDM theory of structure formation, we here use six high-resolution halo simulations performed as part of the Aquarius Project (Springel et al. 2008) to search for subhalos whose properties would allow them, in principle, to host the well observed dSph satellites of the Milky Way. We restrict our attention to the five satellites with abundant, high-quality stellar kinematic data: Fornax, Sculptor, Leo I, Carina, and Sextans (Mateo et al. 2008; Walker et al. 2009). Assuming isotropic velocity dispersions, we identify an Aquarius subhalo with a dark matter potential which results in a good simultaneous fit to each satellite’s photometric and kinematic data.

In addition to focusing specifically on Λ CDM and making direct use of realistic potentials from the Aquarius simulations, our modeling differs from previous work in that we simultaneously fit both photometry and kinematics. We allow for mildly cusped *stellar* profiles with $\rho_\star \sim r^{-a}$ near the centre, where a is in the range 0 to 1. Projections of such profiles are fitted to the photometric data, and with the results in hand we make predictions for the kinematic data, both traditional second moment (line-of-sight velocity dispersion) profiles and full line-of-sight velocity distributions. The latter comparison allows us to test whether simple, spherical, isotropic, Λ CDM-based models are consistent with higher moments of the observed velocity distribution.

For each of the five satellites we study, the best-fitting Aquarius subhalo provides an excellent statistical fit to the data. For four of the five this requires a mildly cusped stellar distribution similar to those found in brighter early-type galaxies. The only galaxy that requires a true core in the star distribution is Leo I, but with such a profile its kinematics are still consistent with a Λ CDM subhalo. We present circular velocity curves for the best-fitting subhalo hosts for each of the MW satellites. Not surprisingly, for a given satellite, the circular velocity curves of “good” subhalos are very similar at the radii that are well sampled by the stellar tracers. This is a consequence of our assumptions of spherical symmetry and isotropy. Finally, we determine the mass of the best-fitting subhalos, both at the time of accretion onto

the host halo and at high redshift, and we show that these quantities have more scatter than the present-day central potentials or maximum circular velocities.

2 THEORETICAL MODELING

The goal of our theoretical modeling is ultimately to compare to the full observed line-of-sight velocity distribution for each satellite. We begin by discussing how to model velocity dispersion profiles and then move on to modeling of the full line-of-sight velocity distribution. In our later analysis, we will use predictions for line-of-sight velocity dispersion profiles to identify possible subhalo hosts for each satellite, and then use the corresponding velocity distributions to check that our isotropic models are indeed consistent with the observed kinematics.

2.1 Velocity dispersion

We assume spherical symmetry both for the potential and for the distribution of stars within it. The line-of-sight velocity dispersion of a dSph satellite at projected radius, R , can then be written as

$$\sigma_{los}^2(R) = \frac{2}{I_\star(R)} \int_R^\infty \left[1 - \beta(r) \frac{R^2}{r^2} \right] \frac{\rho_\star(r) \sigma_r^2 r}{\sqrt{r^2 - R^2}} dr, \quad (1)$$

where $\rho_\star(r)$ is the stellar density profile and $I_\star(R)$ its two-dimensional projection; $\beta = 1 - \sigma_t^2/\sigma_r^2$ is the anisotropy parameter, where $\sigma_t^2(r)$ is the one-dimensional tangential velocity dispersion of the stars and $\sigma_r^2(r)$ the corresponding radial velocity dispersion. These quantities satisfy the radial Jeans equation:

$$r \frac{d(\rho_\star \sigma_r^2)}{dr} = -\rho_\star(r) GM(r)/r - 2\beta(r) \rho_\star \sigma_r^2. \quad (2)$$

The total mass distribution, $M(r)$, is the sum of the mass distributions of dark matter, $M_{dm}(r)$, and stars, $M_\star(r)$.

For our analysis, we use the dark matter mass distributions, $M_{dm}(r)$, of subhalos in the next-to-highest resolution set of Aquarius simulations of galactic halos (level 2 in the notation of Springel et al. (2008)). At the present day, each of the six halos contains about 45000 resolved subhalos within ~ 400 kpc of its centre (corresponding to the radius, r_{50} , of the sphere of mean overdensity 50 times the critical value) with more than 20 particles, each of mass $\sim 10^4 M_\odot$. The structure of each subhalo is well resolved down to a physical radius of ~ 100 pc, corresponding approximately to twice the gravitational softening length (Springel et al. 2008). For radii greater than this convergence radius and less than the radius where the density of bound subhalo mass drops to $\sim 80\%$ of the local total mass density, the subhalos are well fit by an “Einasto” profile,

$$\ln[\rho(r)/\rho_{-2}] = (-2/\alpha)[(r/r_{-2})^\alpha - 1]. \quad (3)$$

Here ρ_{-2} and r_{-2} are the scale density and scale radius (at the point where the density profile has the isothermal slope) respectively, and we take $\alpha = 0.17$ (Navarro et al. 2010). In our kinematic analysis, we extrapolate an Einasto fit to each subhalo when it is necessary to evaluate the mass distribution at radii < 100 pc, and we use the directly determined mass profiles at all larger radii.

To model the three-dimensional stellar density profile, ρ_* , we use functions of the form (Zhao 1997):

$$\rho_*(r) \propto \frac{1}{x^a(1+x^b)^{(c-a)/b}} \quad (4)$$

where $x = r/r_0$ and $\{a, b, c, r_0\}$ are free parameters that will be estimated in the next section by fitting the observed surface density profile of each satellite. We focus on cuspy central profiles ($0 \leq a \leq 1$) because we find that they are required to fit the observed, nearly flat velocity dispersion profiles if we assume isotropic stellar velocity dispersions ($\beta(r) = 0$) and an Einasto halo profile. Although such cuspy profiles have not been used previously in studies of the MW satellites, they are, in fact, required to fit the inner surface brightness profiles of elliptical galaxies of all luminosities, including faint ones (Gebhardt et al. 1996) and so seem *a priori* quite plausible for dSph galaxies also.

If the stellar mass is everywhere negligible compared to the dark matter mass, the projected velocity dispersion in Eq. 2 is independent of the constant of proportionality in Eq. 4 that sets the stellar mass-to-light ratio, M_*/L_* . However, if the stars contribute significantly to the potential of the galaxy, then we must determine the appropriate normalizing factor for Eq. 4 and thus its contribution to the overall mass distribution of the galaxy. For each of the dSphs we will take $M_*/L_* = 1$, consistent with the observational results (Mateo 1998; Coleman et al. 2005). We find that small variations in M_*/L_* , indicative, perhaps, of multiple stellar populations or differences in stellar initial mass function, have little effect on the results we present below.

As also noted above, throughout our analysis we will assume locally isotropic velocity distributions, $\beta(r) = 0$ for all r . This is a strong assumption and it is thus remarkable that we find that we can fit all the kinematic data without relaxing it.

2.2 Velocity Distributions

The preceding discussion demonstrates the well-known fact that the observable quantities $I_*(R)$ and $\sigma_{los}^2(R)$ are insufficient to determine the mass profile, $M(r)$, of a spherical system unless the velocity anisotropy, $\beta(r)$, is specified. Additional kinematic information is contained in higher order moments of the line-of-sight velocity distribution, so appropriate modeling of these moments may constrain $\beta(r)$ and so $M(r)$ (e.g. Gerhard 1993; Lokas & Mamon 2003). A fully consistent dynamical model must clearly match the full line-of-sight velocity distribution at all radii.

If we assume $\beta(r) = 0$, it is possible to invert the observables $I_*(R)$ and $\sigma_{los}^2(R)$ to obtain not only a unique $M(r)$ but also the unique distribution function, $f(\epsilon)$, which reproduces these observables within the potential corresponding to $M(r)$. This distribution function then determines the full line-of-sight velocity distribution at each R . Thus, once we have found a subhalo with $M(r)$ consistent with the $I_*(R)$ and $\sigma_{los}^2(R)$ measurements for a particular dSph, we can check the consistency of the resulting model by comparing its line-of-sight velocity distributions with those observed.

To obtain these velocity distributions, we begin with the Eddington inversion formula,

$$f(\epsilon) = \frac{1}{\sqrt{8}\pi^2} \int_{\epsilon}^0 \frac{d^2\rho_*}{d\Psi^2} \frac{d\Psi}{\sqrt{\Psi-\epsilon}}, \quad (5)$$

where $\epsilon = \Psi(r) + v^2/2$ is the binding energy, Ψ is the gravitational potential, and v is the modulus of the velocity. Potentials for the stars and the dark matter can be separately constructed numerically via the Poisson equation, $\nabla^2\Psi_i = 4\pi G\rho_i$. The indices on potential and density represent a specific component, the dark matter or the stars. The total potential is then the sum of the two.

The Eddington formula in Eq. 5 determines the velocity distribution as a function of the binding energy. However, to compare to observations we need line-of-sight velocity distributions for a set of circular annuli. Defining v_{los} as the component of velocity along the line-of-sight and performing the appropriate weighting over three-dimensional radii r , the distribution of line-of-sight velocities at projected radius R is given by

$$\hat{f}(v_{los}; R) \propto \int_R^{r_{los}} \frac{r dr}{\sqrt{r^2 - R^2}} \int_{\Psi(r)+v_{los}^2/2}^0 f(\epsilon) d\epsilon, \quad (6)$$

where r_{los} is defined by $2\Psi(r_{los}) = v_{los}^2$; for a given velocity v_{los} , we determine r_{los} via a numerical root-finding algorithm. The normalization of Eq. 6 will not be important for the purposes of our discussion.

Once we have determined the velocity distribution in Eq. 6 it is straightforward to construct higher order moments of this distribution. In particular, the n^{th} moment of the distribution is given by

$$\langle v_{los}^n \rangle; R = \frac{\int v_{los}^n \hat{f}(v_{los}; R) dv_{los}}{\int \hat{f}(v_{los}; R) dv_{los}}, \quad (7)$$

where, as in Eq. 6, we have explicitly written \hat{f} as a function of the line-of-sight velocity. As an example that will be important for us below, the RMS velocity determined from Eq. 6 is $\sqrt{\langle v_{los}^2 \rangle; R}$. We are thus able to check our numerical calculation of the velocity distribution function by comparing the RMS velocity determined from Eq. 7 to the equivalent quantity determined from Eq. 1.

Eq. 6 gives the theoretical velocity distribution at R , but in practice, to compare to the observations, we must determine the distribution of \hat{f} at the position of each observed star, and then average it over all the stars in each annulus. Thus, our mean $\hat{f}(v_{los})$ for a given annulus is the mean of the values at the position of the stars, with the individual \hat{f} distributions all normalized to unity. With this procedure there are no approximations related to finite bin size when comparing our theoretical model to the data.

3 DATA ANALYSIS

In this section we perform our analysis of the photometric and kinematic data. We first discuss how we use the star count data to identify parameter values for Eq. 4 that describe each satellite well. We then describe our handling and interpretation of the line-of-sight velocity data, and the way in which we use these data to identify specific Aquarius subhalos that could host each satellite. In particular, we describe the criterion by which we judge goodness-of-fit for a given satellite-subhalo match.

3.1 Photometry

We use photometric data from the following sources for the surface density profiles of our five galaxies: Fornax (Coleman et al. 2005); Sculptor (Battaglia et al. 2008); Sextans (Irwin & Hatzidimitriou 1995); Leo I (Smolcic et al. 2007); Carina (Munoz et al. 2006). Traditional fits to these data sets have used King or Plummer models, the latter corresponding to $\{a, b, c\} = \{0, 2, 5\}$ in Eq. 4. Such fits typically fail to reproduce the measured star counts in the outer regions (Irwin & Hatzidimitriou 1995). In addition, they enforce a constant density core which is consistent with star counts in some globular clusters but not with photometry of the inner regions of brighter early type galaxies, almost all of which show inner cusps corresponding to a values significantly greater than zero (Gebhardt et al. 1996).

We take $\{a, b, c, r_0\}$ in Eq. 4 as free parameters to be adjusted when fitting the observed star count profiles. We perform a standard Abel projection of $\rho_*(r)$ to obtain $I_*(R)$ and we determine the free parameters for each satellite via a standard χ^2 minimization procedure. In performing these fits, we find that there is a complex degeneracy in the space spanned by the four parameters. Motivated by reasons that we discuss in detail in Section 4, we focus on models in which the 3D stellar profiles are characterized by a central shallow cusp and a relatively sharp turnover to a steep outer power law. For Sculptor, Carina, and Sextans we will specifically adopt a central cusp with $a = 0.5$, and $b = 3$, while for Fornax, we will use $a = 1$ and $b = 4$. In Leo I, the star counts do appear to require a core, and we adopt $a = 0$ and a similar transition to the steep outer power law. With a and b fixed *a priori*, we vary the remaining parameters, $\{c, r_0\}$, in order to minimize χ^2 . In all cases this results in reduced χ^2 values near unity, indicating an acceptable fit, and also within the 90% c.l. of the minimum values attainable by varying all four parameters independently. The resulting parameter sets are given together with the corresponding $\chi^2/(N_{bin} - 5)$ in Table 1. Note that since our goal is to demonstrate that the observations are consistent with simple spherical, isotropic models within Λ CDM subhalos, it is not necessary for us to choose the best-fit profile parameters; rather we need only show that the parameters we do choose are consistent with the star count data.

In Figure 1 we plot these surface density profiles for each satellite on top of the observed data. The scale radii vary over the range 0.29 kpc (Carina) $\leq r_0 \leq 0.67 \text{ kpc}$ (Fornax) and the outer slopes over the range 3.3 (Sextans) $\leq c \leq 7.5$ (Leo). As noted above, the degeneracies allow significant variations in these quantities, particularly if a and b are allowed to vary away from the values we have chosen. Our choices are motivated in part by simplicity (e.g. for a), in part by experimentation, determining which parameter ranges allow good fits also to the kinematic data (see below). For Sextans such considerations lead us to settle on a relatively shallow outer density profile, while for Leo the data force us to a steep outer profile. Note that in all cases, the star counts were actually carried out in elliptical annuli. The radial coordinate plotted is the geometric mean of the major and minor axes which we expect to correspond best to the count profile for circular annuli. (The typical ellipticities of these satellites are ~ 0.3 (Irwin & Hatzidimitriou 1995)).

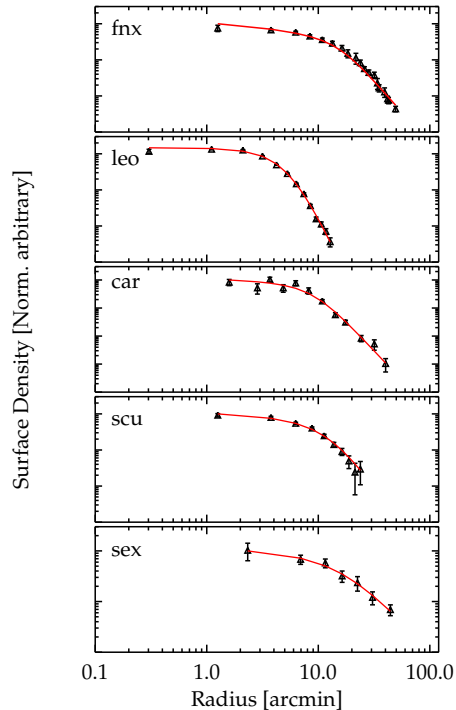


Figure 1. Projected surface density profiles for each of the satellites that we consider, fit using the formula in Eq. 4. The values chosen for the parameters (a, b, c, r_0) for each galaxy are given in Table 1, together with the corresponding χ^2 per degree of freedom. Our procedures for selecting these parameters are outlined in section 3, where we also give references for the observational data plotted in each panel.

3.2 Kinematics

The kinematic datasets that we use consist of line-of-sight stellar velocities from the samples of Mateo et al. (2008) and Walker et al. (2009). The latter use an “Expectation Maximization” method for evaluating membership and removing contaminants from each sample, and we consider only those stars for which Walker et al. (2009) assign $> 90\%$ probability of membership. The resulting numbers of stars are listed in Table 1. For Leo I, which is the only galaxy in our sample without published membership probabilities, we use data from Mateo et al. (2008), and consider those stars as members that have velocities in the range from 240 to 320 km s^{-1} . As this range of velocities is well separated from that of MW foreground stars, it is unlikely that this sample suffers significant contamination. Other methods for cleaning dSphs from contaminating MW halo stars have been considered (e.g. Klimentowski et al. 2007); these typically reduce the velocity dispersion at outer radii. The Walker et al. (2009) membership cuts appear appropriate for our analysis here.

For each satellite, we bin the velocity data in a series of circular annuli and estimate the mean square line-of-sight velocity in each annulus as

$$\hat{\sigma}^2 \equiv \langle v^2 \rangle - \langle v \rangle^2. \quad (8)$$

Here we define the velocity of a star as $v_i = v_{o,i} - \bar{v}_o$, where

$v_{o,i}$ is the observed velocity of the i^{th} star and \bar{v}_o is the mean of these velocities over all stars in the galaxy. The quantity e_i represents the measurement uncertainty of the i^{th} star, and angle brackets represent an average over all the stars in a radial bin. We further assume that the error on \bar{v}_o is negligible and that the actual velocities are uncorrelated with their measurement error. With these assumptions, $\hat{\sigma}^2$ is an unbiased estimator of the corresponding population quantity, and approximating the sampling distributions of $\langle v^2 \rangle$ and $\langle e^2 \rangle$ as normal, the uncertainty on $\hat{\sigma}$ can be estimated as

$$\epsilon^2 = \frac{1}{2N} \frac{\langle v^2 \rangle^2}{\langle v^2 \rangle - \langle e^2 \rangle}. \quad (9)$$

Given an estimate of the intrinsic velocity dispersion profile of each satellite based on Eq. 8, we step through all the subhalos in the six Aquarius simulations to determine which subhalo has the (spherically averaged) potential that best describes the data. Specifically, for each Aquarius subhalo, we derive a spherical potential from the mass profile $M(r)$ and then use the Jeans equation (2) to calculate the line-of-sight velocity dispersion profile, $\sigma_{los}(R)$, which corresponds to the model star count profile of Table 1 and an everywhere isotropic velocity dispersion tensor. This line-of-sight velocity dispersion is then averaged over the positions of all the stars in each annulus to predict the population mean square velocity within that annulus. For each satellite-subhalo pair we then determine the quantity

$$\chi^2 = \sum_{i=1}^{N_{\text{bins}}} \frac{[\hat{\sigma}_i - \sigma_{los}(R_i)]^2}{\epsilon_i^2}, \quad (10)$$

where N_{bins} is the number of annuli and R_i is the mean value of the projected radius of the stars in the i^{th} annulus. For a given satellite, it then follows that the best fitting Aquarius subhalo is the one that minimizes Eq. 10.

Once a “best” subhalo has been identified in this way, we can quantify whether it actually provides an acceptable fit by comparing the χ^2 value from Eq. 10 to the theoretical distribution of χ^2 for N_{bins} degrees of freedom. If p is the fraction of the theoretical distribution at larger values than the measured χ^2 , then we can exclude the hypothesis that the observed satellite has isotropic velocity dispersions and is hosted by this “best” subhalo at confidence level $1 - p$. (Note that, given our assumptions, there are no free parameters when comparing observed and predicted dispersion profiles for a *specific* subhalo.) If p is not very small, then we conclude that the observed satellite could be hosted by a Λ CDM subhalo. Note that the converse does not apply. If p is very small, the observed satellite could still live in a Λ CDM subhalo if it has significant velocity anisotropies.

4 RESULTS

In this section we turn to the implementation of the algorithms described above. We begin by finding the Aquarius subhalo that best matches the line-of-sight velocity dispersion of each satellite under the assumption of negligible velocity anisotropy and for the model stellar density profile we have fitted to the observed counts. We then check whether the line-of-sight velocity distributions of these models are consistent with those observed.

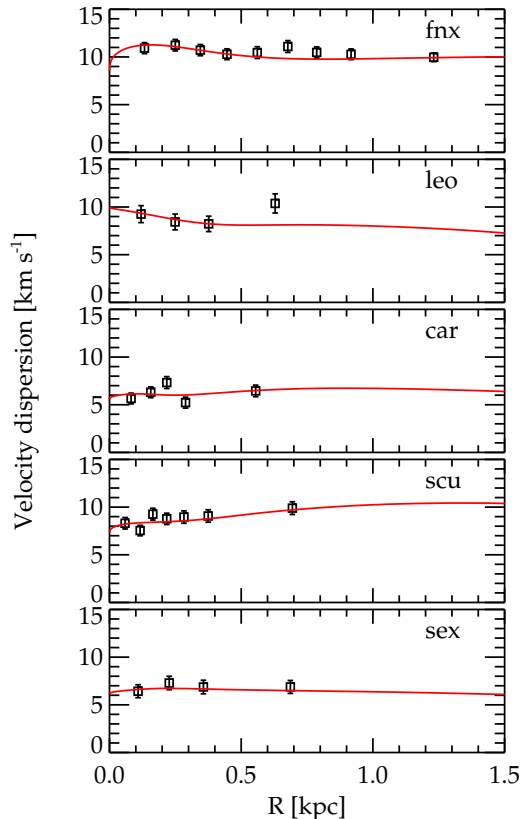


Figure 2. Line-of-sight velocity dispersion for our five satellites. The solid curves show the dispersion predicted by inserting the potential determined from the best fitting Aquarius subhalo and the photometric profile of Table 1 into Eq. 1, assuming no velocity anisotropies. The symbols show the observational data taken from Mateo et al. (2008) (Leo I) and Walker et al. (2009) (Fornax, Carina, Sculptor, and Sextans). The errors on the velocity dispersion in each bin are assigned according to Eq. 9.

Table 1. Number of member stars with measured radial velocities in each of our five galaxies, together with the parameters in Eq. 4 for our preferred fits to their star count profiles, as shown in Fig. 1. The final column gives the value of χ^2 per degree of freedom for these count profile fits.

Satellite	# of stars	a	b	c	r_0 [kpc]	$\chi^2/\text{d.o.f}$
Fornax	2409	1	4	4.5	0.67	1.0
Leo I	328	0	3	7.5	0.40	1.6
Carina	758	0.5	3	5.3	0.29	1.1
Sculptor	1392	0.5	3	5.5	0.32	0.4
Sextans	424	0.5	3	3.3	0.44	0.1

4.1 Best-fitting subhalos

Figure 2 compares the observed velocity dispersion profiles of our five satellites to those predicted by Eq. 2 when a stellar system with a star count profile given by Eq. 4 with the parameters in Table 1, with a stellar mass-to-light ratio of 1, and with negligible velocity anisotropy, is embedded in the Aquarius subhalo that fits best according to the criterion

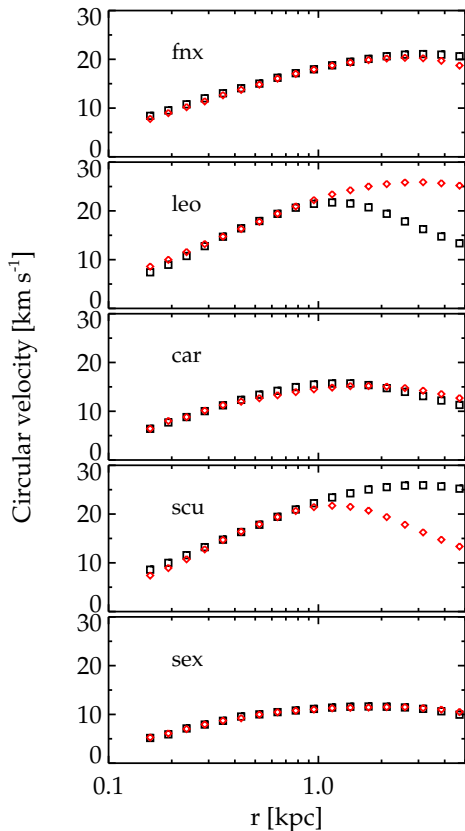


Figure 3. Circular velocity profiles for the best-fitting subhalos (black squares) and the next-best-fitting subhalos (red diamonds) for our five satellites. The symbols give $[GM(r)/r]^{1/2}$ which was used to calculate the potential from the dark matter component in the velocity dispersion profiles of Fig. 2. The profiles of each pair of subhalos are almost identical over the range encompassed by the stellar kinematic data. At larger radii deviations can be large.

of Eq.10. The p-values for these best-fitting subhalos are 0.6, 0.5, 0.6, 0.2 and 0.8 for Fornax, Leo I, Carina, Sculptor, and Sextans, respectively. Thus in all cases the fit appears good from a statistical point of view.

It is important to note that when matching the data in Fig. 2, the photometric parameters chosen in Eq. 4 strongly affect the quality of the fit. For example, for Fornax we are able to find an Aquarius subhalo that matches both the photometry and the kinematics with an acceptable p-value only if $a > 0.8$. This motivates choosing $a = 1$ for this galaxy. For Sculptor, Carina, and Sextans the data constrain the central slope of the stellar density profile less strongly, so for these satellites we choose $a = 0.5$. As noted above, the star count data for Leo I force a value of a close to zero. Hence we pick $a = 0$ for simplicity, although a slightly negative a gives a somewhat better fit to the velocity dispersion data.

In Figure 3, we show circular velocity curves for the two “best” subhalos for each of the satellites; the black squares correspond to the subhalos plotted in Fig. 2. There is essentially no difference between these pairs of curves at radii where we have kinematic data. This reflects the fact that,

for our assumptions, the potential can be derived directly from the observational data so any “acceptably fitting” subhalo will have to resemble the result of this exercise quite closely. At larger radii the potential is effectively unconstrained, however, and the profiles of the two subhalos can differ dramatically. For Fornax, Leo I, Carina, Sculptor and Sextans the maximum circular velocities of the best-fitting subhalos are 21, 22, 16, 26, 12 km s^{-1} , respectively. The corresponding present-day dark matter masses are 7, 2, 2, 15, and $1 \times 10^8 M_{\odot}$.

These results allow us to conclude that the Aquarius simulations include at least one subhalo which is an acceptable host for each of the five satellite galaxies, even under the restrictive assumption of negligible velocity anisotropy. We can extend this analysis to estimate the total number of Aquarius subhalos that are statistically consistent with the kinematic and photometric data for each satellite. Specifically we count those subhalos that have a p-value exceeding 10%. (Remember we are still enforcing isotropic velocity distributions and the specific profile parameters of Table 1). For Fornax we find 13 acceptable subhalos among the six simulations; for Sculptor there are 16 such subhalos; for Carina there are 8 subhalos; for Leo I there are 37; and for Sextans we find over 100 acceptable hosts. For Sextans this large number of hosts is a reflection both of the fact that its velocity dispersion is lower and that the errors on the data are relatively large.

4.2 Full velocity distributions

The preceding analysis shows that Λ CDM subhalo potentials can fit the star count and line-of-sight velocity dispersion profiles of Milky Way satellites to good accuracy, even under the assumption of negligible velocity anisotropy. We now use the techniques described in Section 2 to study if these same models provide good descriptions of the full line-of-sight velocity distributions, for example, of their higher order moments.

The line-of-sight velocity distribution at projected radius R is a convolution of the intrinsic distribution from Eq. 6 with the measurement uncertainty of the stellar velocities. The former has to be averaged over the radial positions of all the stars in each of our annuli, and we model the latter by a Gaussian with dispersion equal to the mean quoted velocity error of these same stars. This measurement uncertainty ranges from $\sim 3 \text{ km s}^{-1}$ for all the Carina bins and the innermost Sculptor bins, down to $\sim 1.5 \text{ km s}^{-1}$ for all the Fornax bins.

The resulting line-of-sight velocity distributions are shown for each of our five galaxies in Fig. 4. For each galaxy we used four circular annuli containing nearly equal numbers of stars. Our motivation for this binning scheme is to retain some information about the variation of distribution shape with radius while keeping a large number of stars in each bin in order to better constrain the shape of the distribution. This results in fewer bins in Fig. 4 than in Fig. 2 for Fornax, Sculptor, and Carina. In each panel of Fig. 4 the solid curve is the line-of-sight velocity distribution calculated as above and normalized to have the same area as the corresponding histogram.

To quantify the level of agreement between model and data in Fig. 4, we compare the distributions of $|v_z|$ in each

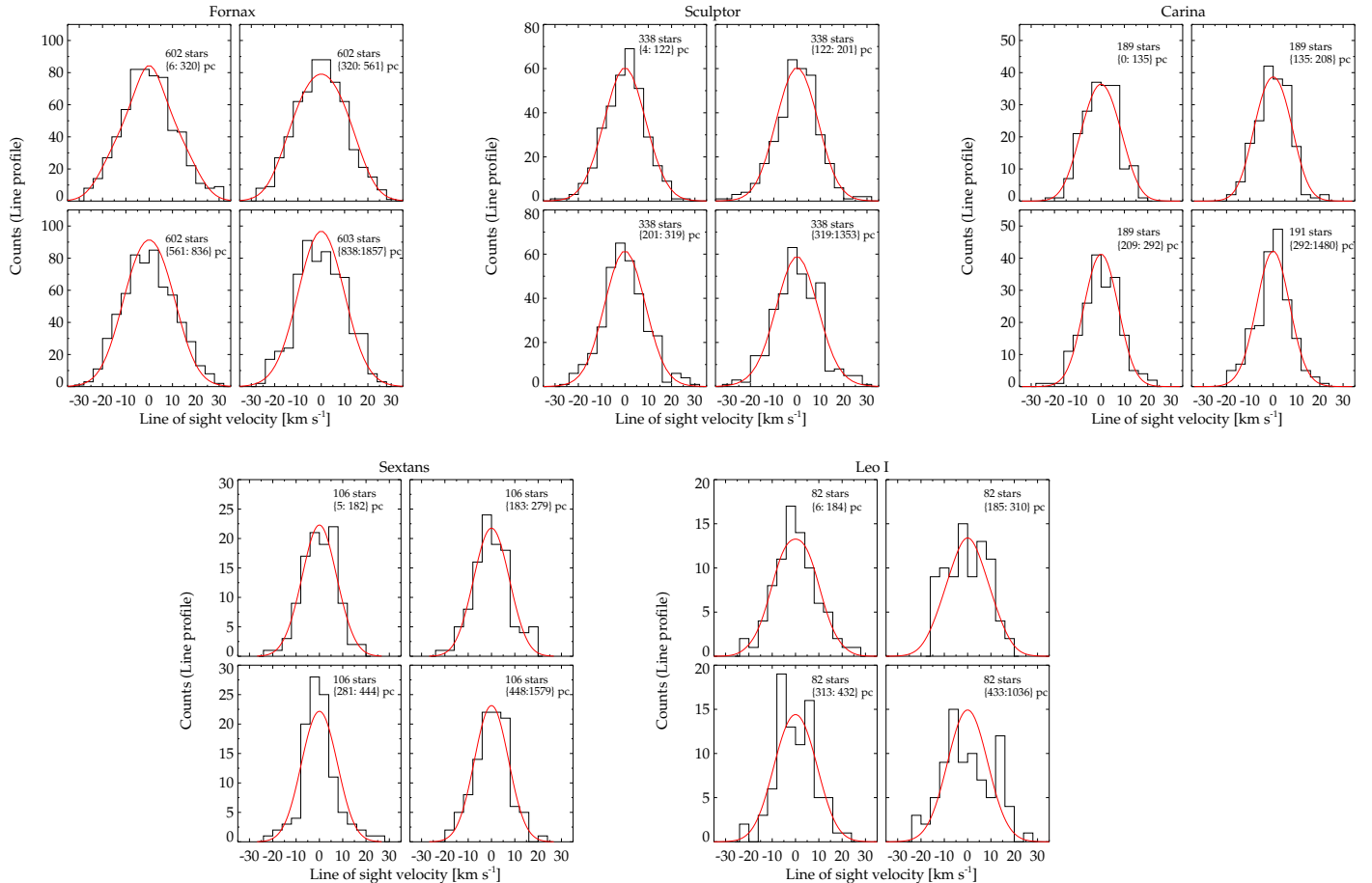


Figure 4. Velocity distributions in four bins for each of our satellites. In each panel, a solid curve shows the theoretical distribution averaged over the radial positions of all the stars in the bin, and then smoothed with a Gaussian representing the typical observational error on the stellar velocities. Labels at the upper right list both the total number of stars in each bin and the approximate radial range they encompass.

panel using a KS test. We take the modulus here because the distribution of the line-of-sight velocity relative to the galaxy mean is expected to be symmetric about zero for *any* equilibrium model (even rotating and/or non-spherical ones) after averaging over a circular annulus. As a result, all shape information is contained in the distribution of $|v_z|$, and restricting the test in this way enhances its sensitivity to higher order moments. The maximum difference between the normalized cumulative distributions of $|v_z|$ for data and model is then a measure of the confidence level at which we can reject the null hypothesis that our simple isotropic, spherical model represents the full, observed line-of-sight velocity distribution in the annulus.

Results of this KS test for each of the four annuli and for all of our satellites are shown in Table 2, with bins 1-4 ordered by increasing radius. These values indicate that our predicted velocity distributions are generally in good agreement with the data. The annuli with the lowest probabilities are bins 3 and 4 of Fornax and bin 4 of Leo I; for Fornax bin 3 and Leo I bin 4 the null hypothesis can be excluded with $> 99\%$ confidence. As can be seen in Fig. 4, the measured line profiles appear less peaked (platykurtic) than the models in these annuli. For Fornax the effect is quite weak,

but is nevertheless significantly detected because of the large number of stars involved. For all the other panels of Fig. 4 differences are less significant and are quite small. Note that the kurtosis of these distributions is expected to be quite sensitive to velocity anisotropy, so the fact that our models fit fairly well can be taken as an indication that anisotropies are probably weak.

A more direct measurement of the kurtosis of the line-of-sight velocity distributions can be obtained by estimating their fourth moment directly. For each annulus, we calculate a sample kurtosis from the N stars it contains as

$$\kappa = \langle v^4 \rangle / \langle v^2 \rangle^2 - 3. \quad (11)$$

The kurtosis is defined so that a Gaussian model gives $\kappa = 0$. We approximate the uncertainty of the sample kurtosis by $\sqrt{24/N}$, the scatter expected for random samples from a normal distribution. For our theoretical model, we calculate second and fourth moments from Eq. 7, after smoothing to account for measurement errors, and we then substitute these into Eq. 11 to obtain the predicted kurtosis.

The results of this exercise are shown in Fig. 5. The models predict very little kurtosis in almost all annuli, and the data agree with this in most cases. Comparing Fig. 5 to

Table 2. KS probabilities for the maximum difference between the observed and modeled cumulative distributions of $|v_z|$ within four equally populated annuli in each of our observed satellites. Bins 1-4 correspond to the annuli of Fig. 4 ordered from inside to outside. The complement of each of these values represents the confidence level at which the hypothesis that the data are drawn from the theoretical distribution can be rejected.

Satellite	bin 1	bin 2	bin 3	bin 4
Fornax	0.05	0.15	0.003	0.02
Leo I	0.46	0.52	0.31	0.003
Carina	0.51	0.44	0.29	0.34
Sculptor	0.32	0.68	0.62	0.67
Sextans	0.41	0.81	0.03	0.97

the second moment data in Fig. 2 clarifies the origin of the discrepancies uncovered by our KS test. For example, in the outer annuli of Fornax, the model distribution is (slightly) narrower than the data while the kurtosis estimates are almost in agreement. For the 4th annulus of Leo I, the model RMS is again smaller than for the data, and the data are more platykurtic. For Leo I, the 2nd annulus also shows a marginally significant platykurtic signal, while for Sextans bin 3 the data are more leptokurtic than the model. However, in the latter two instances the number of stars is too small for the KS test to indicate a significant discrepancy. The rather large bin-to-bin fluctuations in the observational estimates of kurtosis suggest that our Gaussian error bars may be underestimating the true sampling uncertainties.

From this analysis, we conclude that the observed line-of-sight velocity distributions agree surprisingly well with our spherical, isotropic models embedded in Λ CDM subhalo potentials. The remaining differences can plausibly be ascribed to departures from isotropy, from spherical symmetry, from dynamical equilibrium, or (more likely) from a combination of these. Detailed modeling is, of course, necessary to test this possibility, but it is beyond the scope of the present paper. Our main goal here has been to show that simulated Λ CDM halos contain subhalos with potentials consistent with those hosting the observed stellar populations of Milky Way satellites, even if these are assumed to have negligible velocity anisotropy.

5 DISCUSSION AND CONCLUSION

We have investigated whether the gravitational potentials of subhalos in N-body simulations of Λ CDM halo formation are consistent with the high-quality photometric and kinematic data available for five of the brighter satellites of the Milky Way. We find that a direct mapping is, in fact, possible between each of these satellites and a subset of the dark matter subhalos in the six high resolution simulations of the Aquarius Project. Star count profiles with inner cusps scaling as r^{-a} with $0 \leq a \leq 1$ can provide good fits to the observed counts. Placed in the measured Einasto-like potentials of appropriately selected subhalos, they also fit the observed, nearly flat line-of-sight velocity dispersion profiles very well, even under the restrictive assumption of negligible velocity anisotropy. Such isotropic models fit the *shapes*

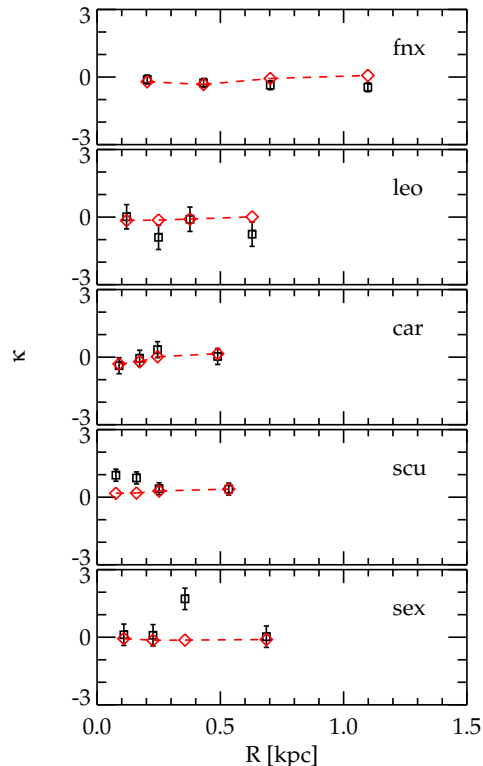


Figure 5. Comparison of the predicted and observed kurtosis of the line-of-sight velocity distribution in four equally populated annuli in each of our five satellites. The kurtosis is defined to be zero for a normal distribution. The black squares are direct observational estimates for each annulus, with errors given by $\sqrt{24/N}$, where N is the number of stars. The red diamonds are theoretical predictions from our isotropic models after convolution with the measurement errors and averaging over the stellar positions in each annulus.

of the observed line-of-sight velocity distributions well, in addition to their second moments.

We have measured the present-day maximum circular velocities of the “best-fit” subhalos for each of these five satellites. These range from 10 to 30 km s^{-1} . Subhalos consistent with hosting the observed systems at $z = 0$ have peak circular velocities (i.e. the largest maximum circular velocity they *ever* had) ranging from 12 to 50 km s^{-1} . The maximum past masses of the main progenitors of these subhalos range up to $\sim 5 \times 10^9 M_{\odot}$, while their masses at $z = 7$ (the approximate lower bound on the redshift of reionization (Dunkley et al. 2009)) range up to $\sim 10^9 M_{\odot}$. At $z = 0$ their Galactocentric distances range from 40 to 400 kpc.

Our results indicate that current data on faint Milky Way satellites are consistent with these galaxies living in Λ CDM halos. They do not, however, explain *why* galaxies living in such subhalos should have the observed properties. Exploring this issue is an important task for future work (e.g. Li et al. 2010; Cooper et al. 2009; Sawala et al. 2010; Okamoto & Frenk 2009; Busha et al. 2010).

ACKNOWLEDGMENTS

We thank Matt Walker for helpful discussions and for making the velocity data for the satellites publically available. We thank V. Smolcic and G. Battaglia for providing Leo I and Sculptor photometry data respectively. We also thank Jie Wang for assistance with the Aquarius simulations data. The Aquarius project is part of the programme of the Virgo Consortium for cosmological simulations. Support for LS for this work was provided by NASA through Hubble Fellowship grant HF-51248.01-A awarded by the Space Telescope Science Institute, which is operated by the Association of Universities for Research in Astronomy, Inc., for NASA, under contract NAS 5-26555. CSF acknowledges a Royal Society Wolfson Research Merit Award. This work was also supported in part by an STFC rolling grant to the ICC.

REFERENCES

- Aaronson M., 1983, *Astrophys. J.*, 266, L11
 Angus G. W., Diaferio A., 2009, *Mon. Not. Roy. Astron. Soc.*, 396, 887
 Battaglia G., Helmi A., Tolstoy E., Irwin M., Hill V., Jablonka P., 2008, *Astrophys. J.*, 681, L13
 Busha M. T., Alvarez M. A., Wechsler R. H., Abel T., Strigari L. E., 2010, *Astrophys. J.*, 710, 408
 Coleman M. G., Da Costa G. S., Bland-Hawthorn J., Freeman K. C., 2005, *Astron. J.*, 129, 1443
 Cooper A. P., et al., 2009, arXiv:0910.3211
 Dunkley J., et al., 2009, *Astrophys. J. Suppl.*, 180, 306
 Evans N. W., An J., Walker M. G., 2009, *Mon. Not. Roy. Astron. Soc.*, 393, L50
 Gebhardt K., et al., 1996, *Astron. J.*, 112, 105
 Gerhard O. E., 1993, *Mon. Not. Roy. Astron. Soc.*, 265, 213
 Gilmore G., et al., 2007, *Astrophys. J.*, 663, 948
 Goerdt T., Moore B., Read J. I., Stadel J., Zemp M., 2006, *Mon. Not. Roy. Astron. Soc.*, 368, 1073
 Hogan C. J., Dalcanton J. J., 2000, *Phys. Rev.*, D62, 063511
 Irwin M., Hatzidimitriou D., 1995, *Mon. Not. Roy. Astron. Soc.*, 277, 1354
 Kazantzidis S., Zentner A. R., Kravtsov A. V., 2006, *Astrophys. J.*, 641, 647
 Klimentowski J., et al., 2007, *Mon. Not. Roy. Astron. Soc.*, 378, 353
 Li Y., De Lucia G., Helmi A., 2010, *Mon. Not. Roy. Astron. Soc.*, 401, 2036
 Lokas E. L., 2009, *Mon. Not. Roy. Astron. Soc.*, 394, L102
 Lokas E. L., Mamon G. A., 2003, *Mon. Not. Roy. Astron. Soc.*, 343, 401
 Mateo M., 1998, *Ann. Rev. Astron. Astrophys.*, 36, 435
 Mateo M., Olszewski E. W., Pryor C., Welch D. L., Fischer P., 1993, *Astron. J.*, 105, 510
 Mateo M., Olszewski E. W., Walker M. G., 2008, *Astrophys. J.*, 675, 201
 Munoz R. R., et al., 2006, *Astrophys. J.*, 649, 201
 Navarro J. F., et al., 2010, *Mon. Not. Roy. Astron. Soc.*, 402, 21
 Navarro J. F., Frenk C. S., White S. D. M., 1996, *Astrophys. J.*, 462, 563
 Navarro J. F., Frenk C. S., White S. D. M., 1997, *Astrophys. J.*, 490, 493
 Okamoto T., Frenk C. S., 2009, *Mon. Not. Roy. Astron. Soc.*, 399, L174
 Sánchez-Salcedo F. J., Reyes-Iturbide J., Hernandez X., 2006, *Mon. Not. Roy. Astron. Soc.*, 370, 1829
 Sawala T., Scannapieco C., Maio U., White S., 2010, *Mon. Not. Roy. Astron. Soc.*, 402, 1599
 Smolcic V., et al., 2007, *Astron. J.*, 134, 1901
 Springel V., et al., 2008, *Mon. Not. Roy. Astron. Soc.*, 391, 1685
 Stadel J., et al., 2009, *Mon. Not. Roy. Astron. Soc.*, 398, L21
 Strigari L. E., Bullock J. S., Kaplinghat M., 2007, *Astrophys. J.*, 657, L1
 Strigari L. E., et al., 2006, *Astrophys. J.*, 652, 306
 Strigari L. E., et al., 2008, *Nature*, 454, 1096
 Tremaine S., Gunn J. E., 1979, *Phys. Rev. Lett.*, 42, 407
 Walker M. G., et al., 2009, *Astrophys. J.*, 704, 1274
 Walker M. G., Mateo M., Olszewski E. W., Gnedin O. Y., Wang X., Sen B., Woodroffe M., 2007, *Astrophys. J.*, 667, L53
 Walker M. G., Mateo M., Olszewski E. W., Sen B., Woodroffe M., 2009, *Astron. J.*, 137, 3109
 Wilkinson M. I., Kleyna J., Evans N. W., Gilmore G., 2002, *Mon. Not. Roy. Astron. Soc.*, 330, 778
 Wolf J., et al., 2009, arXiv:0909.2995
 Zhao H., 1997, *Mon. Not. Roy. Astron. Soc.*, 287, 525